# Enhanced electrocatalytic activity and stability of Ce doping NiFe layered double hydroxide for alkaline Seawater oxidation

Luhuan Yang, Bifeng Wang, Meilan Xu, Lingfeng Li, Qinglan Ye*, Xuetang Xu, Fan Wang*

School of Chemistry & Chemical Engineering, Guangxi University, Guangxi Key Laboratory of Electrochemical Energy Materials, Nanning 530004, China.
Email: yeql@gxu.edu.cn; fanwang@gxu.edu.cn

## EXPERIMENTAL SECTION

### Chemicals and Materials.

Commercial Ni foam (NF) was purchased from Changsha Liyuan New Materials Co. $Fe_2(SO_4)_3 \cdot 9H_2O$, $NiSO_4 \cdot 6H_2O$, $Ce(NO_3)_3 \cdot 6H_2O$, urea (≥ 99.5%) and $NH_4F$ (≥ 99.5%) were purchased from Sinopharm Chemical Reagent Co., Ltd. All the reagents were of analytical grade and used as received without any further purification.

### Synthesis of NiFeCe LDH on Ni foam substrate with various Ce doping level

NiFeCe LDH electrodes with various Ce level doping shared the same synthetic route, while the feeding amounts of $Ce(NO_3)_3$ are 0.05, 0.10, 0.15, and 0.20 mmol, respectively. The as-obtained electrode was denoted as $NiFeCe_x$ LDH, and x represent represents the feeding molar amount of $Ce(NO_3)_3$.

### Material Characterizations.

The morphological information was obtained by scanning electron microscopy (SEM, Hitachi SU8200) and transmission electron microscopy system (TEM, FEI Tecnai F30). X-ray diffraction (XRD) characterization was performed on a Rigaku D/MAX 2500V instrument (Rigaku Corporation, Japan) with a scanning speed of 4° $min^{-1}$ in the 2θ range of 10−70°. The chemical valence states and compositions were analyzed by X-ray photoelectron spectroscopy (XPS) on an Thermo SCIENTIFIC Nexsa instrument, with the C 1s binding energy (284.8 eV) as the calibration reference.

The compositions of Ni, Fe, and Ce were analyzed by inductively coupled plasma optical emission spectroscopy (ICP-OES) on a Plasma 2000 full-spectrum ICP spectrometer.

**Electrochemical Performance Tests**

Electrochemical measurements were performed in a 1.0 M KOH solution or simulated seawater (1.0 M KOH + 0.5 M NaCl) solution using a DH7002 electrochemical workstation (Jiangsu Donghua Analytical Instrument Co., Ltd.) and a standard three-electrode system, while platinum sheet, Hg/HgO electrode, and the NF-supported nanosheet arrays served as counter electrode, reference electrode and working electrode, respectively. The potential was calibrated to the reversible hydrogen electrode (RHE) by using the following equation:

$$E_{RHE}(V) = (E_{Hg/HgO} + 0.0591) \times pH + 0.098 \quad (1)$$

Linear sweep voltammetry (LSV) polarization curves were collected at a scan rate of 5 mV $s^{-1}$ with 90% iR compensation. The overpotential ($\eta$) was calculated as:

$$\eta = E_{RHE} - 1.23\ V \quad (Eq.2)$$

The apparent Tafel slope was derived from the polarization curve by fitting experimental data to Equation (3):

$$\eta = a + b \log j \quad (Eq.\ 3)$$

where $a$ is the Tafel constant, $b$ is the Tafel slope, and $j$ is the steady−state current density.

The double-layer capacitance ($C_{dl}$) was determined through cyclic voltammetry (CV) curves measured at different scan rates in the non-faradaic region. The electrochemical active surface area (ECSA) was calculated using the formula $ECSA = C_{dl}/C_s$, where $C_s$ is the specific capacitance of a smooth surface under alkaline conditions, typically taken as 40 μF $cm^{-2}$.

Electrochemical impedance spectroscopy (EIS) experiments were performed over a frequency range of 0.01 Hz to $10^5$ Hz. The long-term stability of the electrocatalyst was assessed using galvanostatic mode. The turnover frequency (TOF) was calculated according to $TOF = (J \times A)/(4 \times F \times n)$, where J (A $cm^{-2}$) is the current density at a given

overpotential, A ($cm^2$) is the surface area of the electrode material, 4 is the number of electrons transferred per mole of oxygen generated in the OER, F is the Faraday constant (96485.3 C $mol^{-1}$), and n (mol) represents the molar number of Ni, Fe and Ce ions in NiFeCe LDH or NiFe LDH (without considering NF substrate), which was determined by ICP-OES. The stability of the catalyst was tested at a constant current density of 500 mA $cm^{-2}$.

**Density Function Theory (DFT) calculation method**

For all DFT calculations, the Vienna Ab initio Simulation Package (VASP) was employed, and the Perdew-Burke-Ernzerhof (PBE) functional and projector-augmented wave (PAW) method were applied to describe the exchange-correlation energy and electron-ion interactions. All slab models contain atomic layers and a vacuum layer of 15 Å thickness to avoid artificial interaction between periodic images. To accurately describe the strong electronic correlations in the 3d orbitals of transition metals, the DFT+U method was employed. Structural optimizations, including both atomic positions and unit cell parameters, were performed using the Broyden–Fletcher–Goldfarb–Shanno (BFGS) algorithm as implemented in ASE. The UnitCellFilter was applied to allow for the simultaneous relaxation of atomic coordinates and cell dimensions. To improve the description of van der Waals interaction, DFT-D3 correction was employed. The energy cutoff was set to be 500 eV. The Brillouin zone was sampled by Gamma-centered k-point with 3 × 3 × 1. The structures were fully relaxed until the maximum force on each atom was less than 0.03 eV/Å, and the energy convergent standard was $10^{-5}$ eV.

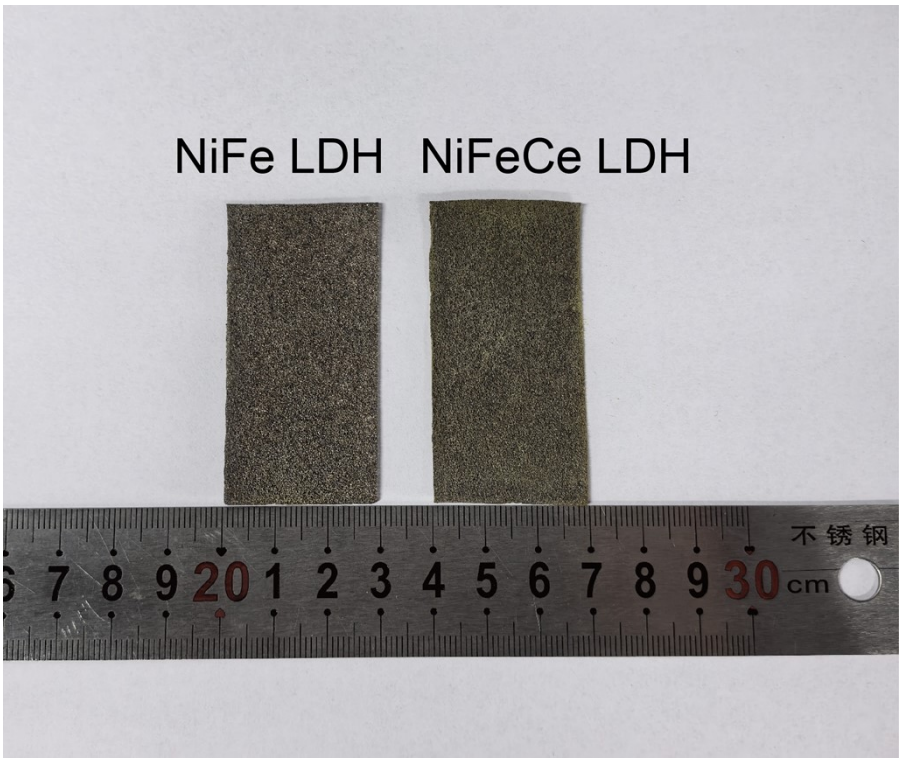


Figure S1. Photograph of NiFe LDH and NiFeCe LDH electrode with large size.

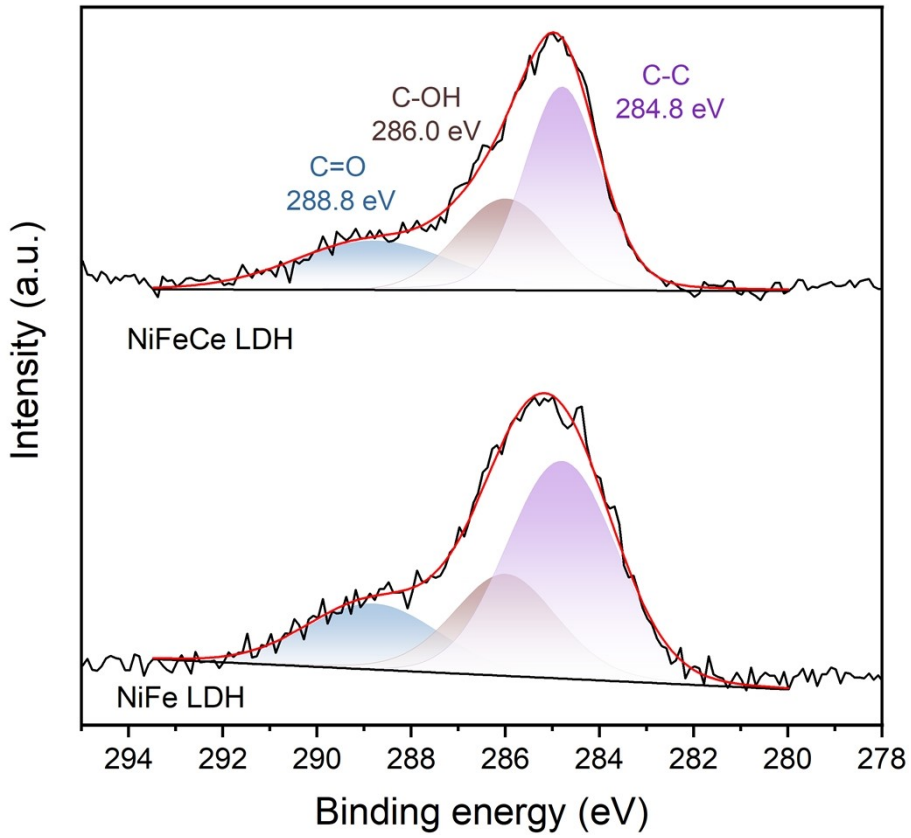


Figure S2. C 1s XPS spectra of NiFe LDH and NiFeCe LDH electrodes.

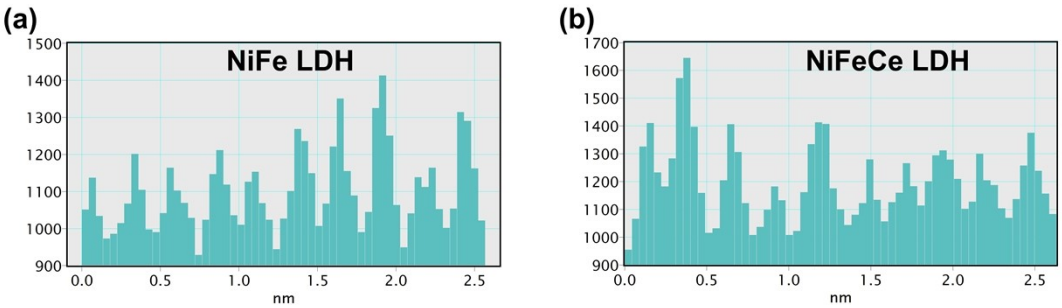


Figure S3. The line intensity profiles from HRTEM images. (a) NiFe LDH. (b) NiFeCe LDH.

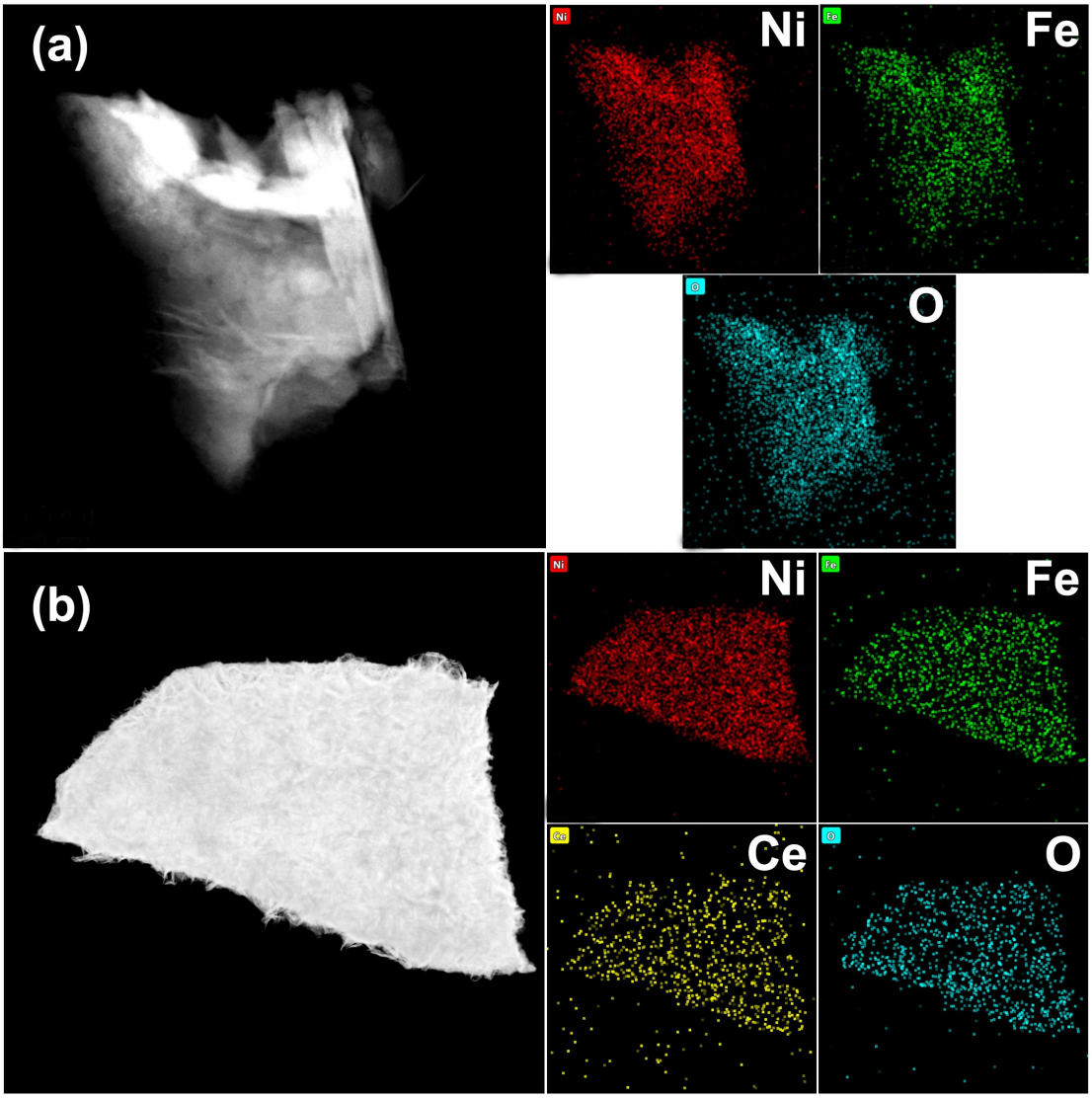


Figure S4. Elemental mapping of (a) NiFe LDH and (b) NiFeCe LDH nanosheets.

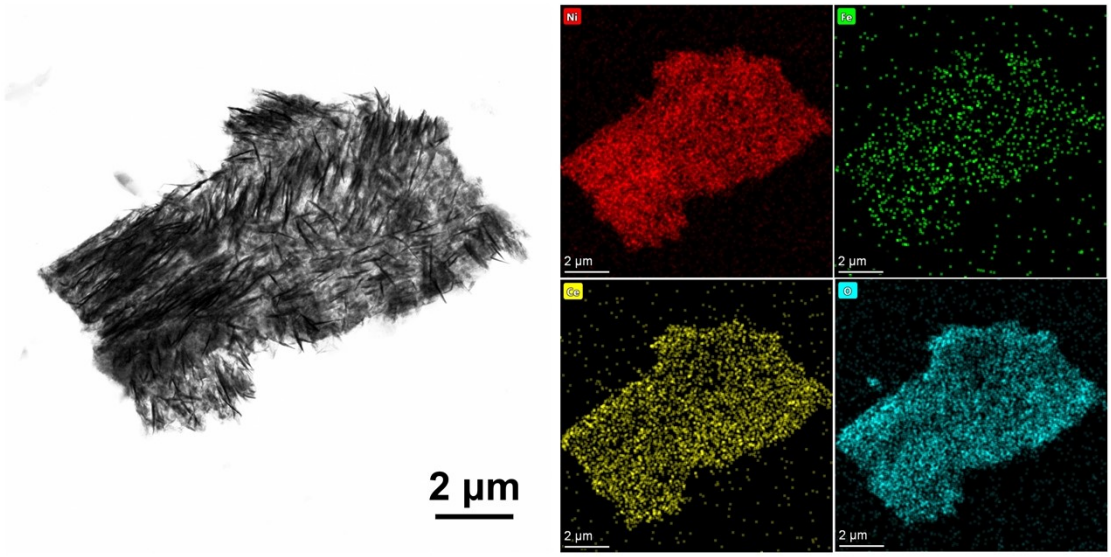


Figure S5. TEM and element mapping of NiFeCe LDH nanosheet.

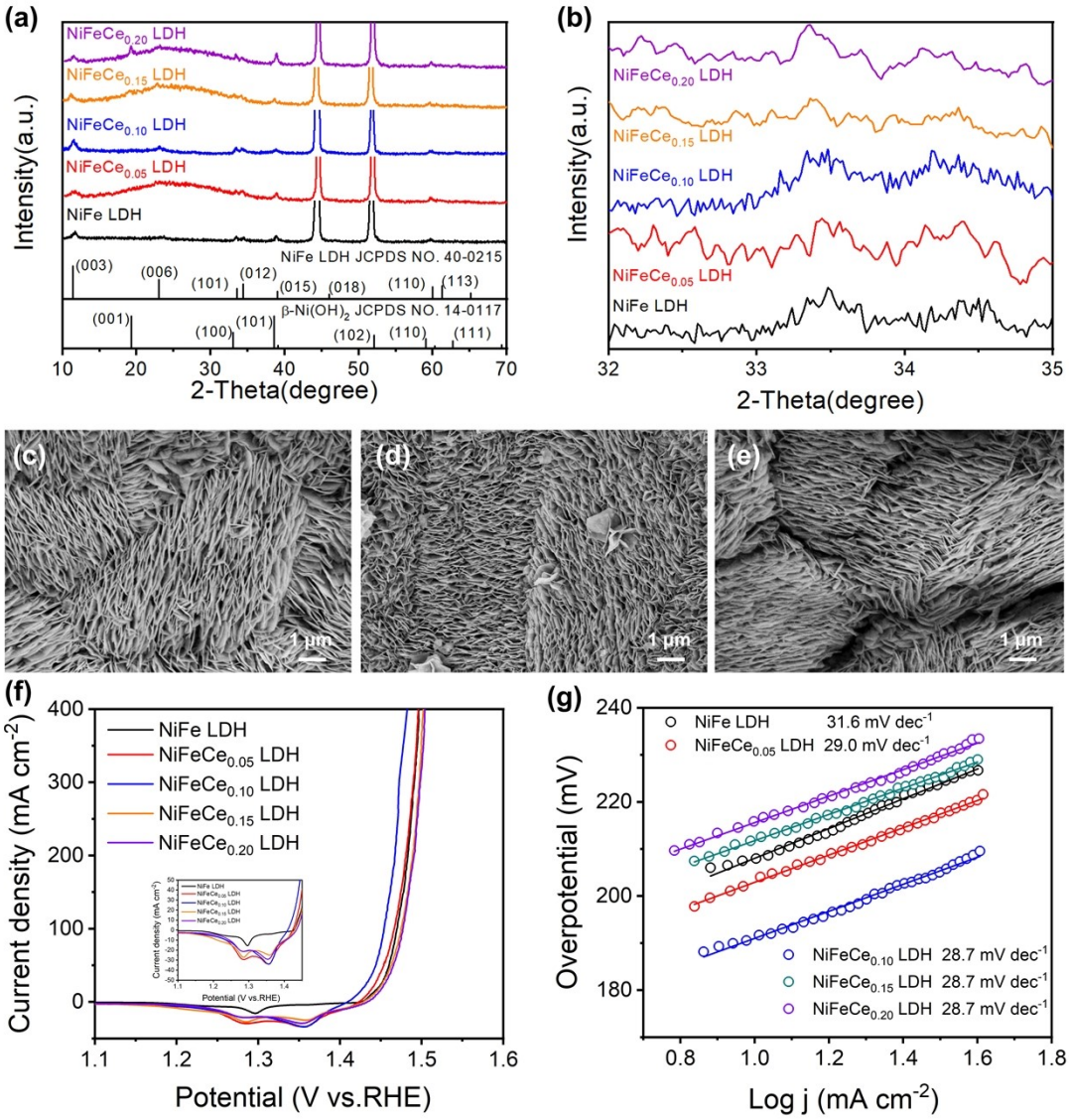


Figure S6. (a) XRD patterns and (b) the corresponding enlarged part of the NiFeCe LDH prepared with different Ce feeding amounts. SEM images of (c) $NiFeCe_{0.05}$ LDH, (d) $NiFeCe_{0.15}$ LDH and (e) $NiFeCe_{0.20}$ LDH. (f) Linear sweep voltammetry (LSV) curves and (g) Tafel plots for the oxygen evolution reaction (OER) performance of NiFeCe LDH prepared with different Ce feeding amounts. The subscript number of Ce represents the feeding molar amount of $Ce(NO_3)_3$. $NiFeCe_{0.10}$ LDH was selected as the representative research object in this work due to its optimal performance.

All NiFeCe layered double hydroxide (LDH) electrodes with varying Ce contents exhibit similar layered structures, as evidenced by the (003) diffraction peak appearing in the small-angle region (Figure S6a). However, at high Ce doping levels, the

formation of the β-$Ni(OH)_2$ phase becomes prominent, indicating that Ce doping disrupts the deposition of NiFe LDH. In the enlarged sections of the XRD patterns, the (101) and (012) peaks shift toward smaller angles with increasing Ce content, confirming the effective incorporation of Ce (Figure S6b). SEM images reveal quasi-parallel alignment of the as-obtained nanosheet arrays, suggesting similar growth behavior across the NiFeCe LDH nanosheets (Figure S6c-S6e). Thus, differences in their catalytic activity are primarily attributable to intrinsic activity.

The LSV curves of all NiFeCe LDH electrodes are shown in Figure S6f. $NiFeCe_{0.10}$ LDH electrode achieves the lowest overpotential of 199 mV at a current density of 20 mA $cm^{-2}$. However, the difference in the overpotential among the electrodes are rather small, while the $NiFeCe_{0.20}$ LDH electrode delivers the highest overpotential of 223 mV. The similar tafel slopes in Figure S6g also reveal the similar OER kinetics.

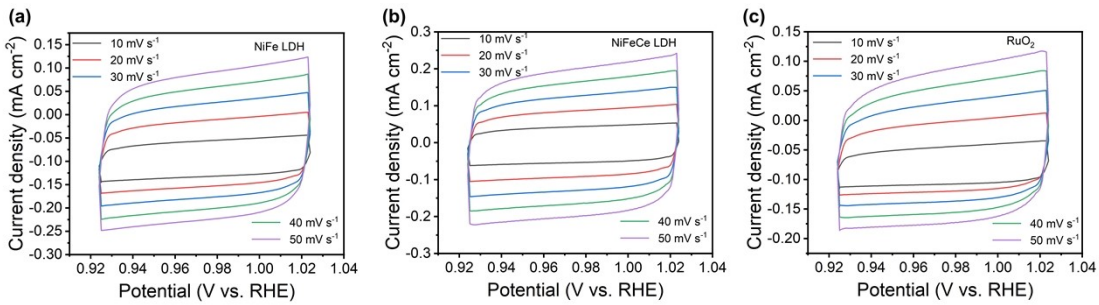


Figure S7. Cyclic voltammetry (CV) curves of the electrodes at non-faradic region. (a) NiFe LDH; (b) NiFeCe LDH; (c) $RuO_2$.

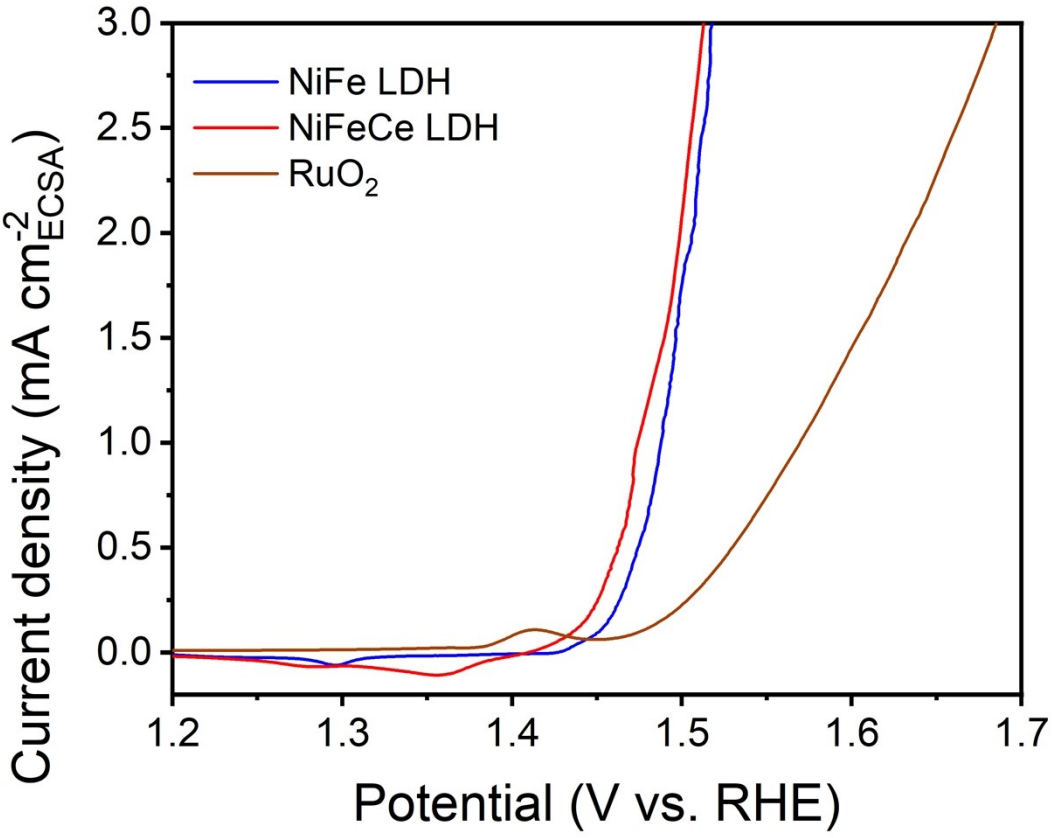


Figure S8. ECSA-normalized LSV curves of the as-obtained electrodes.

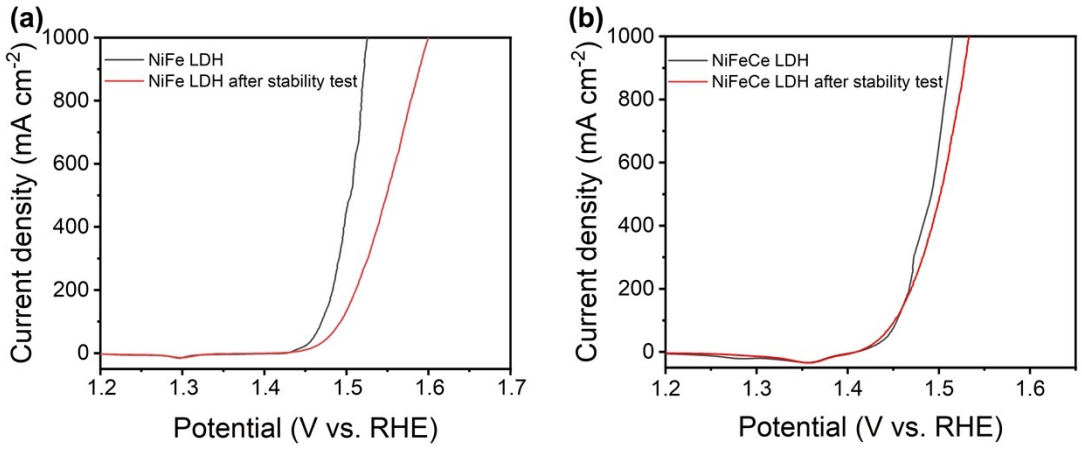


Figure S9. LSV curves of (a) NiFe LDH and (b) NiFeCe LDH electrodes before and after stability testing.

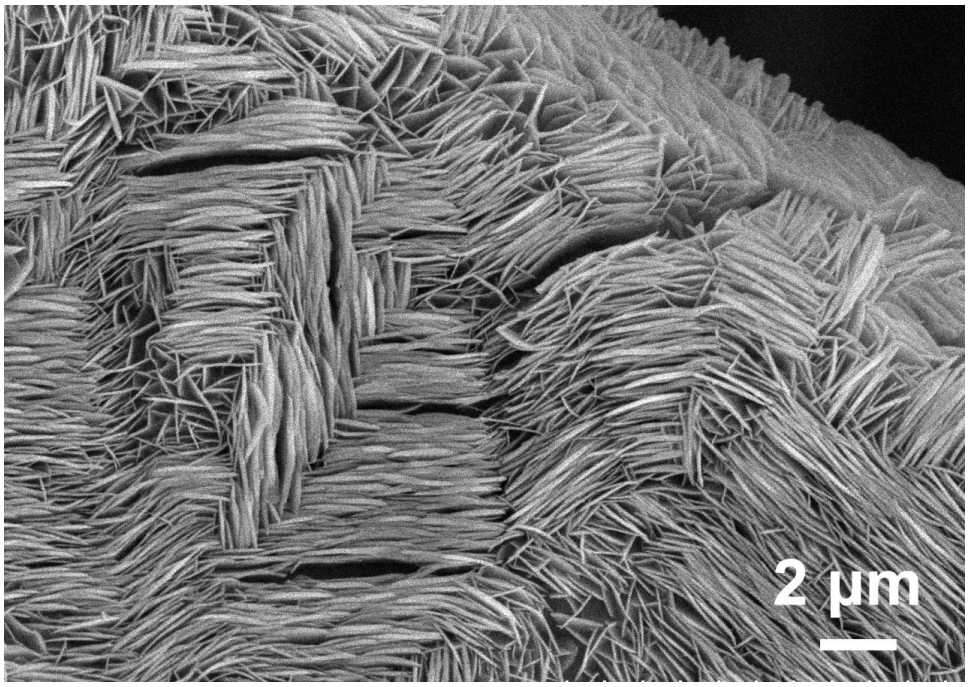


Figure S10. SEM image of NiFe LDH electrode after stability test.

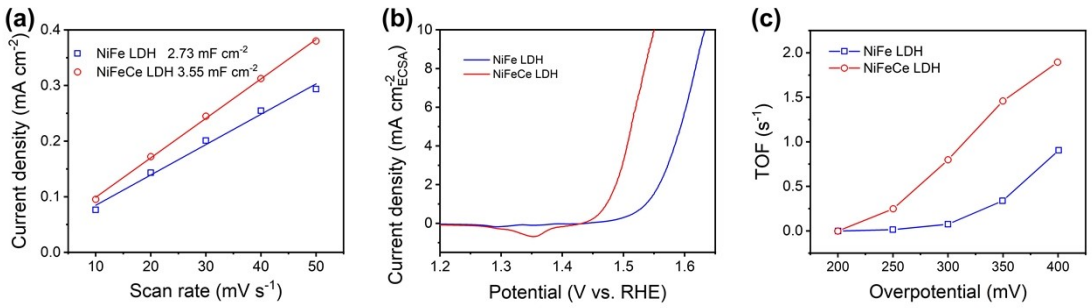


Figure S11. (a) Relationship between scan rate and Δ*j* for verifying the Cdl values, (b) corresponding ECSA- normalized LSV curves, and (c) the TOF plots of NiFe LDH and NiFeCe LDH electrodes in simulated seawater electrolyte.

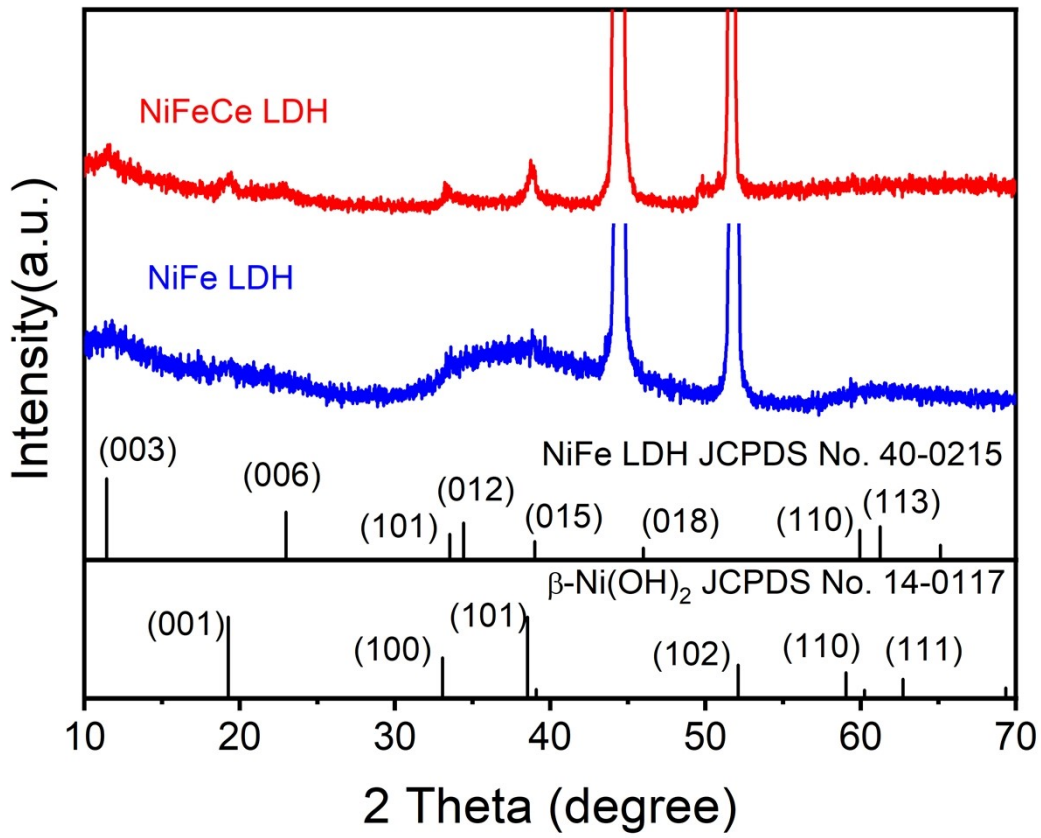


Figure S12. XRD pattern of the NiFe LDH and NiFeCe LDH electrodes after stability test in simulated seawater electrolyte.

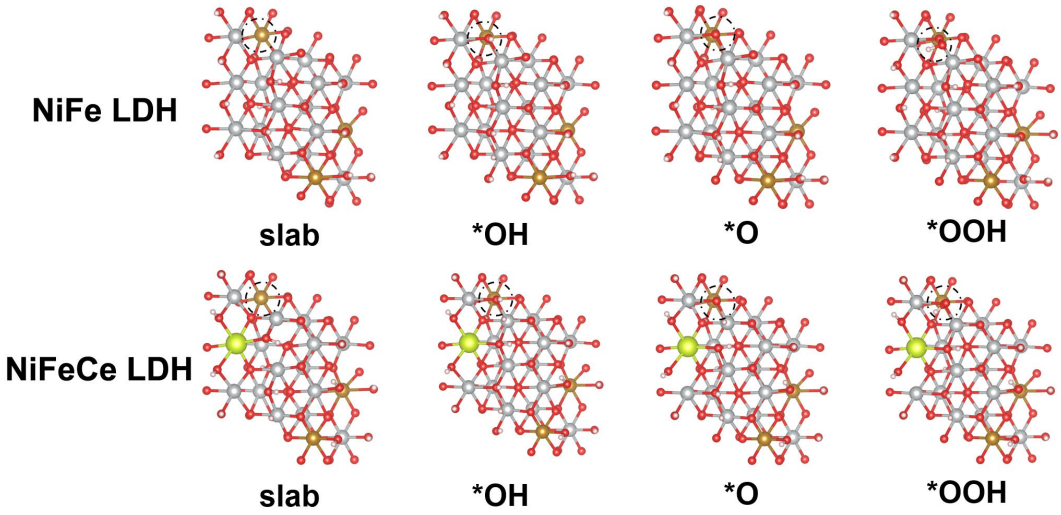


Figure S13 Illustration of the adsorption OER intermediates occurred on NiFe LDH and NiFeCe LDH.

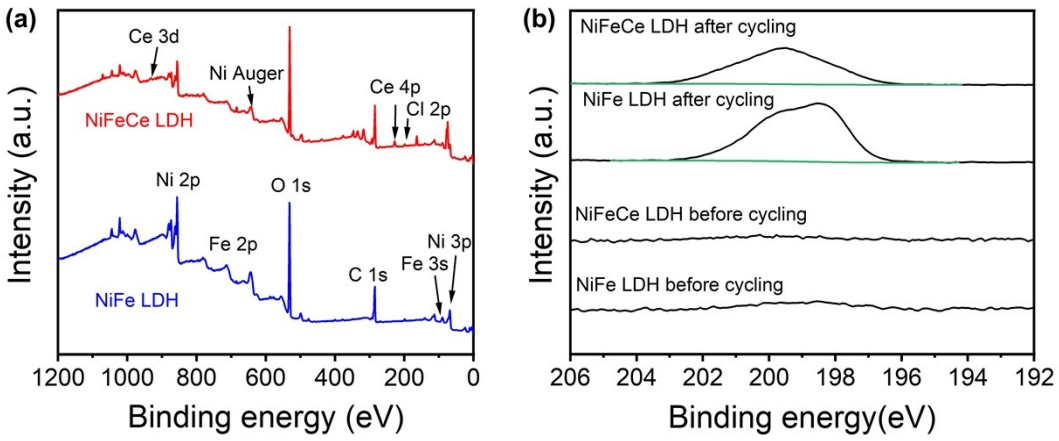


Figure S14. (a) XPS survey spectra of the NiFe LDH and NiFeCe LDH electrodes after stability test in simulated seawater electrolyte. (b) Cl 2p XPS spectra of the NiFe LDH and NiFeCe LDH electrodes before and after stability test in simulated seawater electrolyte.

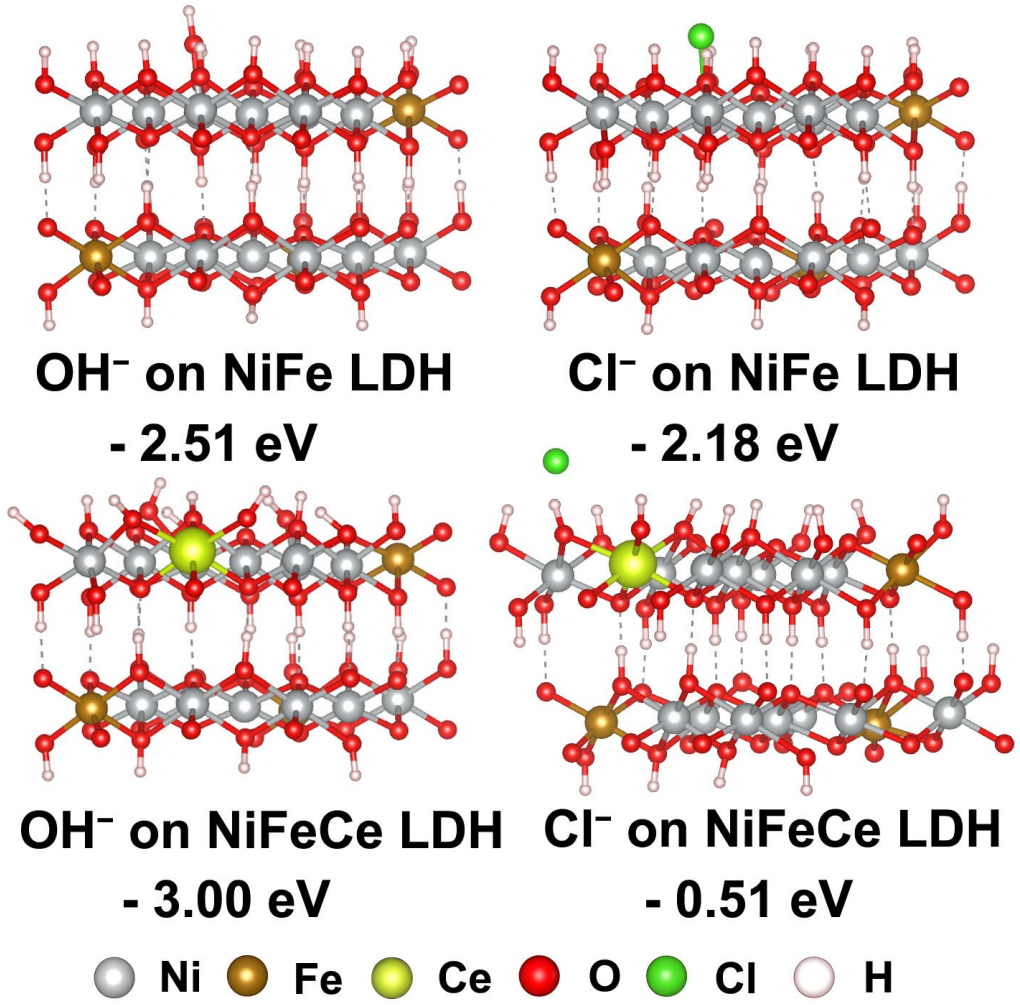


Figure S15. Scheme of adsorption models and the corresponding adsorption energies of $OH^-$ and $Cl^-$ anions on NiFe LDH and NiFeCe LDH.

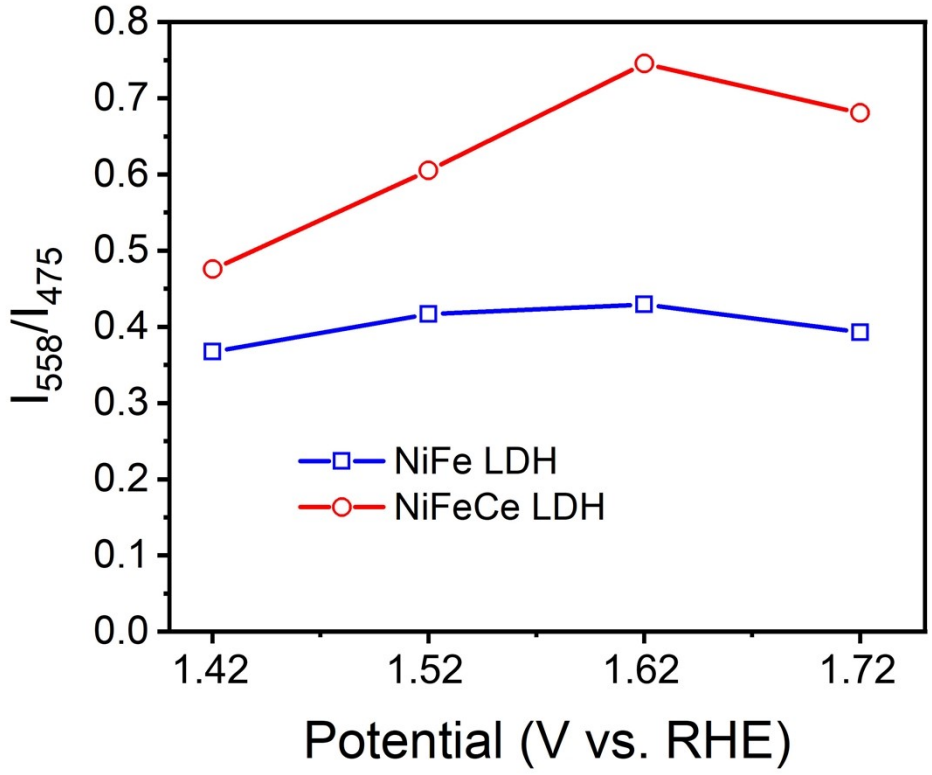


Figure S16. The $I_{558}/I_{475}$ intensity ratio of NiOOH signal at the potential range of 1.42 to 1.72 V (vs. RHE).

Table S1. Content ratio of metal element in NiFeCe LDH and NiFe LDH based on ICP-OES and XPS analysis.

| Sample | Fe/Ni | | Ce/Fe | |
|---|---|---|---|---|
| | ICP-OES | feed ratio | ICP-OES | feed ratio |
| NiFe-LDH | 0.098 | 0.125 | / | / |
| NiFeCe-LDH | 0.102 | 0.125 | 0.021 | 2.5 |

Table S2. Comparison of OER performance for selected nickel-iron based electrocatalysts.

| Electrocatalyst | η / mV | | | | Tafel slope / (mV $dec^{-1}$) | Durability time/h | Ref. |
|---|---|---|---|---|---|---|---|
| | 10 mA $cm^{-2}$ | 100 mA $cm^{-2}$ | 500 mA $cm^{-2}$ | 1000 mA $cm^{-2}$ | | | |
| NiFeCe LDH | 191 | 224 | 262 | 285 | 28.7 | 1000 | This work |
| IrNi@NiFe-MOFs | 228 | 335 | / | / | 37.6 | 115 | [1] |
| NiFe-S-0.6 | 213 | 252 | 294 | | 32 | 260 | [2] |
| Hf-NiFe-LDH/NF | 230 | 258 | / | / | 30 | 90 | [3] |
| Te-$NiFeO_xH_y$/NF | 208 | 270 | 310 | | 21.7 | 300 | [4] |
| NiFe/MnNiCo-LDH | 227 | 265 | / | / | 64.14 | 50 | [5] |
| NiFe(S)/NM | / | 310 | 370 | | 41.4 | 500 | [6] |
| E-NiFe | 243 | / | / | | 52 | 24 | [7] |
| Ru/NiFe-LDH-40/NF | 208 | 271 | / | / | 30 | 100 | [8] |
| NiFe-LDH/$MoS_{2-0.25}$ | / | 284 | 336 | | 37.34 | 24 | [9] |
| Co-B/NiFe-LDH | 244 | / | / | / | 56 | 50 | [10] |
| NiFe@NiB | 280 | / | / | / | 42.3 | 120 | [11] |
| Sn-NiFeOOH@NF | 223 | 270 | / | / | 41.9 | 200 | [12] |
| NiFe-AL@$Mo_2CT_x$ | 230 | 300 | / | / | 53 | 50 | [13] |
| Rh@NiFe-MIL-53 | 240 | 334 | / | / | 48.2 | 110 | [14] |
| $Ni_{0.85}Se$@NiFe LDH | 225 | / | / | / | 41.4 | 40 | [15] |
| $Ir_{SA}$-NiFe LDH/NiMo | / | 260 | 350 | | 24 | 500 | [16] |

Table S3. Equivalent circuit fitting results of EIS.

| Electrocatalyst | Impedance (Ω) | | |
|---|---|---|---|
| | $R_s$ | $R_f$ | $R_{ct}$ |
| NiFeCe LDH | 1.265 | 0.041 | 0.546 |
| NiFe LDH | 1.378 | 0.265 | 3.385 |
| $RuO_2$ | 1.443 | 0.054 | 8.946 |
| NiFeCe LDH in simulated seawater electrolyte | 1.981 | 0.063 | 0.772 |
| NiFe LDH in simulated seawater electrolyte | 2.887 | 0.311 | 3.712 |

Table S4. Content ratios of $Ni^{3+}/Ni^{2+}$ and $Fe^{3+}/Fe^{2+}$ before and after stability test in 1 M KOH solution and in simulated seawater electrolyte.

| Sample | Before stability test | | After stability test in 1 M KOH solution for 1000 h | | After stability test in simulated seawater electrolyte | |
|---|---|---|---|---|---|---|
| | $Ni^{3+}/Ni^{2+}$ | $Fe^{3+}/Fe^{2+}$ | $Ni^{3+}/Ni^{2+}$ | $Fe^{3+}/Fe^{2+}$ | $Ni^{3+}/Ni^{2+}$ | $Fe^{3+}/Fe^{2+}$ |
| NiFe-LDH | 0.477 | 0.913 | 0.568 | 2.248 | 0.655 | 1.708 |
| NiFeCe-LDH | 0.632 | 0.875 | 0.725 | 0.906 | 0.782 | 1.458 |

Table S5. Comparison of OER performance of the present electrocatalyst with the reported nickel-iron based electrocatalysts in 1 M KOH + 0.5 M NaCl electrolyte.

| Electrocatalyst | η / mV | | | TOF / $s^{-1}$ | Tafel slope / (mV $dec^{-1}$) | durability | Ref. |
|---|---|---|---|---|---|---|---|
| | 100 mA $cm^{-2}$ | 500 mA $cm^{-2}$ | 1000 mA $cm^{-2}$ | | | | |
| NiFeCe LDH/NF | 244 | 288 | 331 | 0.78@300 mV | 21.6 | 600 h | This work |
| Sn-NiFeOOH@NF | 340 | / | / | / | 63.3 | 200 h | [12] |
| NF/FeCoP/NiFe LDH | 256 | / | / | / | 89.9 | 55 h | [17] |
| NiTe@NiFe-LDH/NF | 277 | 359 | / | / | 59.79 | 50 h | [18] |
| TS-NiFe LDH/NF | / | 333 | 398 | 2.89@ 410 mV | / | 350 h | [19] |
| Li-NFL/CN | 284 | / | / | 0.148@280 mV | / | 25 h | [20] |
| NiFe LDH-CeW@NFF | / | 330 | 386.7 | 0.54@300 mV | 66 | 100 h | [21] |
| NiFe LDH-CNA3 | 264 | / | / | 0.195@270 mV | / | 72 h | [22] |
| CoP@NiFe LDH | 260 | / | / | / | 44.4 | 24 h | [23] |
| NiFe LDH@PCM/NF | 266 | 314 | 344 | 0.75@270 mV | 38.67 | 500 h | [24] |
| $NiFe_4$-VOx/NF | 284 | / | / | / | / | 100 h | [25] |
| POM-CoFe LDH/NF | 265 | 325 | 368 | ~ 1.2@300 mV | / | 1300 h | [26] |
| NiFe LDH/NF (in $PF_6^-$-containing seawater) | / | 247 | 282 | ~ 0.17@at 270 mV) | 28.7 | 5000 h | [27] |
| NiFePBA/$Ni(OH)_2$/NF | 216 | 339 | 361 | / | 49.09 | 1000 h | [28] |
| $Ce(OH)_3$@NiFe LDH/NF | / | 295 | 321 | 0.67@315 mV | 23.5 | 1000 h | [29] |

Table S6. Metal ion concentrations in the electrolyte after stability test.

| Stability test | Electrode | Concentration of elements in the electrolyte | | |
|---|---|---|---|---|
| | | Ni ($mg\ L^{-1}$) | Fe ($mg\ L^{-1}$) | Ce ($mg\ L^{-1}$) |
| In KOH solution for 1000 h | NiFe LDH | 0.068 | 0.085 | |
| | NiFeCe LDH | 0.035 | 0.061 | 0.035 |
| In simulated seawater electrolyte for 500 h | NiFe LDH | 8.963 | 0.233 | |
| | NiFeCe LDH | 0.012 | 0.197 | 0.317 |

**Reference**


[1] J. Jia, Y. Wang, Y. Cha, Z. Wang, J. Huang, D. Wang, H. Li, K. Guo, J. Li, J. Huang, Boosting OER Performance of NiFe-MOFs via Heterostructure Engineering: Promoted Phase Transformation and Self-optimized Dynamic Interface Electron Structure, Advanced Functional Materials, 2025, 35, 2500568. https://doi.org/10.1002/adfm.202500568.

[2] L. He, N. Wang, M. Xiang, L. Zhong, S. Komarneni, W. Hu, S-vacancy-rich NiFe-S nanosheets based on a fully electrochemical strategy for large-scale and quasi-industrial OER catalysts, Applied Catalysis B: Environment and Energy, 2024, 345, 123686. https://doi.org/10.1016/j.apcatb.2023.123686.

[3] J. Wang, M. Wang, Z. Lu, J. Xie, J. Huang, J. Hu, Y. Cao, Multielectronic synergetic Hf-doped NiFe-LDH/NF for efficient bifunctional electrocatalytic OER/UOR, International Journal of Hydrogen Energy, 2024, 82, 724-732. https://doi.org/10.1016/j.ijhydene.2024.07.426.

[4] Y. Li, H. Guo, J. Zhao, K. Pang, R. Song, Rapid surface reconstruction of Te-doped NiFe layered double hydroxide for robust oxygen evolution at high current density, ACS Sustainable Chemistry & Engineering, 2024, 12(32), 12101-12112. https://doi.org/10.1021/acssuschemeng.4c03672.

[5] G. Zhao, L. Mu, L. Chen, H. Chen, W. Liao, N. Zhao, B. Zhang, M. Du, T. Zhang, Construction of NiFe/MnNiCo-LDH heterostructure for enhanced oxygen evolution reaction for efficient water splitting, International Journal of Hydrogen Energy 2024, 88, 432-440. https://doi.org/10.1016/j.ijhydene.2024.09.114.

[6] Q. Li, W. Luo, X. Cui, J. Shi, Rapid and In Situ Active Sites Regeneration for OER Activity Recovery and Greatly Prolonged Water-Splitting Performance, Angewandte Chemie International Edition, 2025, 137(21), e202500303. https://doi.org/10.1002/anie.202500303.

[7] B. Zhang, Y. Ji, D. Shi, S. Wang, P. Zhang, S. Zhang, F. Lu, Ultrasonic-assisted structural engineering of NiFe-LDH nanosheets: Unraveling the mechanistic enhancements in alkaline OER for green electrocatalysis, Journal of Electroanalytical Chemistry, 2025, 981, 118958.

https://doi.org/10.1016/j.jelechem.2025.118958.

[8] H.-L. Jia, Y.-J. Lu, K.-C. Liu, Y. Teng, M. Guan, S. Zhou, Ru doped NiFe-LDH based on self-supporting electrode as efficient and stable OER electrocatalyst for alkaline water-splitting, Dalton Transactions, 2025, 54, 18026-18037. https://doi.org/10.1039/d5dt02409a.

[9] X. Li, Y. Qin, B.-y. Zhang, B.-y. Zhang, R.-d. Zhao, J. Li, D. Zhao, L.-h. Miao, Rose-like NiFe-LDH/$MoS_2$ Electrocatalysts Achieve 1000 mA $cm^{-2}$ OER with Enhanced Charge Transfer and Seawater Stability, Crystal Growth & Design, 2025, 25(20), 8616-8630. https://doi.org/10.1021/acs.cgd.5c01006.

[10] L. Li, L. Xiao, X. Cheng, S. Li, T. Tian, Y. Wang, H. Tang, NiFe-LDH modified cobalt boride for enhanced OER catalytic performance, Electrochimica Acta, 2025, 539, 147094. https://doi.org/10.1016/j.electacta.2025.147094.

[11] J. Lim, S. Jo, H. Oh, P. Choi, J. Oh, K. Seo, H.-Y. Park, K. Eom, A phase-optimized NiFe-LDH/NiB heterostructure as an efficient and durable oxygen evolution electrocatalyst in alkaline media, Journal of Materials Chemistry A, 2025,13(39), 33479-33489. https://doi.org/10.1039/d5ta04549e.

[12] L. Xiao, X. Bai, Z. Wang, C. Hou, J. Guan, Electron redistribution in Sn-NiFe oxyhydroxides for overall seawater electrolysis, Chemical Engineering Journal, 2025, 521, 166872. https://doi.org/10.1016/j.cej.2025.166872.

[13] H.-X. Yang, W. Xu, P.-W. Zhong, D. Zhang, Z. Yu, B. Li, H. Wang, Y. Cao, H.-F. Wang, H. Yu, Coupling NiFe alloy/LDH and $Mo_2CTx$ MXene for enhanced oxygen evolution, Journal of Energy Chemistry, 2025, 105, 121-129. https://doi.org/10.1016/j.jechem.2025.01.048.

[14] J. Jia, J. Zhang, K. Guo, L. Zhang, G. Du, H. You, J. Huang, M. Tu, H. Li, Y. Peng, Deciphering the role of ultra-low-loaded rhodium in NiFe-MIL-53 for superior oxygen evolution reaction, Journal of Energy Chemistry, 2025, 100, 77-86. https://doi.org/10.1016/j.jechem.2024.08.022.

[15] T. Wang, H. Wei, R. Hu, N.-N. Liang, Z. Sun, J. Qin, M. Luo, Y. Yang, Edge-Selected Selenization of Subnanometer Amorphous NiFe Hydroxides for Efficient Alkaline Oxygen Evolution, ACS Nano, 2025, 19(38), 34017-34029.

https://doi.org/10.1021/acsnano.5c09887.

[16] Y. Wu, M. Chen, H. Sun, T. Zhou, X. Chen, G. Na, G. Qiu, D. Li, N. Yang, H. Zheng, Coupling Ir single atom with NiFe LDH/NiMo heterointerface toward efficient and durable water splitting at large current density, Applied Catalysis B: Environment and Energy, 2025, 360, 124548. https://doi.org/10.1016/j.apcatb.2024.124548.

[17] Y. Lu, W. Peng, W. Zhang, W. Li, J. He, D. Zhou, W. Hu, Collaborative promotion of water/seawater electrolysis performance by the in-situ generated phosphate anions and $Fe^{3+}$ in FeCoP/NiFe LDH heterostructure, International Journal of Hydrogen Energy, 2025, 118, 102-112. https://doi.org/10.1016/j.ijhydene.2025.03.231.

[18] X. Ju, X. He, Y. Sun, Z. Cai, S. Sun, Y. Yao, Z. Li, J. Li, Y. Wang, Y. Ren, Fabrication of a hierarchical NiTe@ NiFe-LDH core-shell array for high-efficiency alkaline seawater oxidation, Iscience, 2024, 27(1), 108736. https://doi.org/10.1016/j.isci.2023.108736.

[19] H. Wang, Z. Li, S. Hong, C. Yang, J. Liang, K. Dong, H. Zhang, X. Wang, M. Zhang, S. Sun, Tungstate intercalated NiFe layered double hydroxide enables long-term alkaline seawater oxidation, Small, 2024, 20(28), 2311431. https://doi.org/10.1002/smll.202311431.

[20] Z. Li, M. Liu, J. Yan, L.Y.S. Lee, A "doping–interfacing" strategy enables efficient alkaline freshwater and seawater oxidation by NiFe-layered double hydroxides, Chemical Engineering Journal, 2023, 473, 145293. https://doi.org/10.1016/j.cej.2023.145293.

[21] M. Li, H.-J. Niu, Y. Li, J. Liu, X. Yang, Y. Lv, K. Chen, W. Zhou, Synergetic regulation of $CeO_2$ modification and $(W_2O_7)^{2-}$ intercalation on NiFe-LDH for high-performance large-current seawater electrooxidation, Applied Catalysis B: Environment and Energy, 2023, 330, 122612. https://doi.org/10.1016/j.apcatb.2023.122612.

[22] J. Cai, X. He, Q. Dong, Y. Li, P. Su, D. Qu, J. Liu, Y. Lu, Q. Jin, Z. Sun, Employing shielding effect of intercalated cinnamate anion in NiFe LDH for stable and

efficient seawater oxidation, Surfaces and Interfaces, 2024, 51, 104772. https://doi.org/10.1016/j.surfin.2024.104772.

[23] Z. Zhang, K. Ye, H. Du, X. Li, In situ electrodeposition synthesis of CoP@ NiFe LDH heterostructure as high-performance electrocatalyst for enhanced seawater electrolysis, International Journal of Hydrogen Energy, 2024, 62, 722-731. https://doi.org/10.1016/j.ijhydene.2024.02.202.

[24] Z. Li, W. Zuo, C. Liu, C. Yang, Z. Cai, S. Sun, M. Yue, M. Zhang, X. Wang, H. Wang, Polycalmagite Coating Enables Long-Term Alkaline Seawater Oxidation Over NiFe Layered Double Hydroxide, Small, 2025, 21(13), 2408642. https://doi.org/10.1002/smll.202408642.

[25] Y. Yao, S. Chen, Y. Feng, Y. Wang, J. Xiong, Y. Zhao, Two-dimensional MOF derived NiFe-VOx with high catalytic activity and corrosion resistance for seawater splitting, Applied Catalysis A: General, 2025, 705, 120448. https://doi.org/10.1016/j.apcata.2025.120448.

[26] Tang, J. Nan, X. Zhou, H. Luo, B. Ying, Q. Yu, F. Luo, B. Tang, X. Sun, Engineered PW12-polyoxometalate docked Fe sites on CoFe hydroxide anode for durable seawater electrolysis, Nature Communications, 2025, 16, 5541.

[27] X. He, Y. Yao, L. Zhang, H. Wang, H. Tang, W. Jiang, Y. Ren, J. Nan, Y. Luo, T. Wu, F. Luo, B. Tang, X. Sun, Hexafluorophosphate additive enables durable seawater oxidation at ampere-level current density, Nature Communications, 2025, 16, 4998.

[28] X. He, Y. Cheng, Q. Zhang, T. Yan, K. Dong, Y. Yao, J. Nan, Y. Zhou, X. Guo, D. Zheng, S. Sun, J. Zhao, B. Ying, F. Luo, B. Tang, X. Sun, Structural evolution and self-reconstruction of nickel hexacyanoferrate Prussian blue analogues for long-lasting ampere-current seawater oxidation, Nano Today, 2024, 58, 102454.

[29] 33 X. Fang, C. Ye, W. Zhuang, Y. Yang, S. Hong, S. Sun, X. He, F. A. Ibrahim, M. S. Hamdy, F. Gong, Y. Yao, X. Sun, W. Hu, High-Coverage $Ce(OH)_3$-Decorated NiFe Layered Double Hydroxide for Durable Seawater Oxidation at Ampere-Scale Current Densities, Small 2025, 21, 2505219